

The Viscous Evolution of White Dwarf Merger Remnants

Josiah Schwab^{1,2}, Ken J. Shen^{3,2*}, Eliot Quataert^{1,2}, Marius Dan⁴, Stephan Rosswog^{4,5}

¹*Physics Department, University of California, Berkeley, CA 94720, USA*

²*Astronomy Department and Theoretical Astrophysics Center, University of California, Berkeley, CA 94720, USA*

³*Lawrence Berkeley National Laboratory, Berkeley, CA 94720, USA*

⁴*School of Engineering and Science, Jacobs University Bremen, Campus Ring 1, 28759 Bremen, Germany*

⁵*Astronomy and Oskar Klein Centre, Stockholm University, AlbaNova University Center, SE-106 91 Stockholm, Sweden*

Revision 14d303d6b4932970c3c841f0dc0f1807d7b5c92c

ABSTRACT

The merger of two white dwarfs (WDs) creates a differentially rotating remnant which is unstable to magnetohydrodynamic instabilities. These instabilities can lead to viscous evolution on a time-scale short compared to the thermal evolution of the remnant. We present multi-dimensional hydrodynamic simulations of the evolution of WD merger remnants under the action of an α -viscosity. We initialize our calculations using the output of eight WD merger simulations from Dan et al. (2011), which span a range of mass ratios and total masses. We generically find that the merger remnants evolve towards spherical states on time-scales of hours, even though a significant fraction of the mass is initially rotationally supported. The viscous evolution unbinds only a very small amount of mass ($\lesssim 10^{-5} M_{\odot}$). Viscous heating causes some of the systems we study with He WD secondaries to reach conditions of nearly dynamical burning. It is thus possible that the post-merger viscous phase triggers detonation of the He envelope in some WD mergers, potentially producing a Type Ia supernova via a double detonation scenario. Our calculations provide the proper initial conditions for studying the long-term thermal evolution of WD merger remnants. This is important for understanding WD mergers as progenitors of Type Ia supernovae, neutron stars, R Coronae Borealis stars and other phenomena.

Key words: white dwarfs - hydrodynamics - supernovae: general

1 INTRODUCTION

Systems consisting of two white dwarfs (WDs) are natural outcomes of binary stellar evolution. These binaries are not static; absent any other torques the loss of angular momentum via gravitational wave (GW) emission will drive the binary together. Programs such as the SWARMS survey (Mullally et al. 2009) and the ELM survey (Brown et al. 2010) have dramatically increased the number of known WD binaries, including some systems which will merge within a Hubble time (Kilic et al. 2012). The Galactic population of WD binaries is expected to be a source of unresolved GW foregrounds at mHz frequencies, though only a handful of presently known systems would be individually detectable by a space-based GW interferometer mission (Nelemans 2009).

Details of the inspiral, in particular whether tidal torques cause the binary to be synchronized and the location of the tidal heating, are active areas of inquiry that

can have a significant impact on the dynamics of the binary and the thermal state of the WDs (Fuller & Lai 2012). As the orbital separation shrinks, the less massive (and hence larger) WD will eventually overflow its Roche lobe and begin transferring mass to the companion. The stability of this mass transfer depends on e.g., whether the material forms a disc or flows directly onto the companion, which in turn depends on the mass ratio (q) and total mass (M_{tot}) of the binary (e.g. Marsh et al. 2004).

Those systems which do undergo unstable mass transfer and subsequently merge have been of substantial theoretical interest. In particular, such systems have received attention as the possible progenitors of Type Ia supernovae (Iben & Tutukov 1984; Webbink 1984). Considerable work exists exploring this “double degenerate” scenario and recent observational results have begun to favor it (e.g. Bloom et al. 2012; Schaefer & Pagnotta 2012). Another possibility is that double white dwarf binaries with total masses exceeding the Chandrasekhar mass undergo accretion induced collapse to form a neutron star (e.g. Saio & Nomoto 1985). Less massive double degenerate systems are likely to have non-explosive

* Einstein Fellow

outcomes and have been invoked to explain objects like the R Coronae Borealis stars and extreme helium stars (Webbink 1984; Saio & Jeffery 2000; Clayton et al. 2007).

An accurate simulation of the merger process requires a 3D code without prescribed geometry and with good numerical conservation properties. For these reasons, the pioneering study of Benz et al. (1990) used smoothed particle hydrodynamics (SPH). More recent studies (e.g. Dan et al. 2011; Raskin et al. 2012; Pakmor et al. 2012) have improved on these first results by contributing additional physics, more accurate initial conditions, higher resolution and more sophisticated numerical techniques. These simulations follow the evolution of the binary through the tidal disruption of one of the components. In some cases the merger is sufficiently violent that an explosion may result (Pakmor et al. 2010; Dan et al. 2012). When the merger itself does not trigger an explosion, some material from the disrupted lower mass WD forms a shock-heated layer at the surface of the primary WD while the rest of the material forms a thick disc at larger radii.

The evolution of such systems has frequently been treated in the literature as a long-lived ($\sim 10^5$ yr) phase of accretion from a disc at the Eddington limit (e.g. Nomoto & Iben 1985). This picture was improved by Yoon et al. (2007), who considered accretion at a similar rate but onto a hot envelope, and by van Kerkwijk et al. (2010), who made simple α -disc estimates of the accretion time-scale and found it to be far more rapid (\sim hours) than the time-scale for accretion at the Eddington limit.

Recently, Shen et al. (2012) provided a new model of the different evolutionary phases of WD merger remnants. They argued that the evolution is much more “star-like” than the accretion disc oriented models that have dominated the literature. More concretely, Shen et al. (2012) showed that the rapid dynamical evolution of the merger ($\sim 10^2$ s) gives way to a longer lived viscous phase driven by magnetohydrodynamic instabilities ($\sim 10^4 - 10^8$ s) before the onset of a long ($\sim 10^4$ yr) thermal phase. In contrast with previous work, this implies that the long term evolution of a white dwarf merger remnant is not determined by accretion, but rather by the internal redistribution of heat/momentum and the external cooling rate of the viscously heated, nearly shear-free remnant.

In Shen et al. (2012), the viscous evolution was calculated in 1D using a γ -law equation of state. The goal of this work is to refine the understanding of the outcome of the viscous evolution of WD merger remnants using higher dimensional numerical simulations. In addition, we consider a wider variety of WD+WD systems than Shen et al. (2012), who focused on roughly Chandrasekhar mass CO+CO mergers.

In §2 we outline the numerical methods we use, including how we construct our initial conditions from simulations by Dan et al. (2011). In §3 we present the results of each of our calculations. §4 provides a discussion of the end states of the calculations. In §5 we state our conclusions and propose avenues for future work. In an Appendix, we show various test calculations that confirm the results we focus on in the main text.

2 NUMERICAL METHODS

We perform our calculations using the ZEUS-MP2 (Hayes et al. 2006) code, a massively parallel implementation of the algorithms used in the ZEUS family of codes. These codes solve the fluid equations using finite differences on a staggered mesh. The internals of ZEUS are well-documented in the literature (for example, Stone & Norman 1992). While there have been other, more modern developments in astrophysical fluid codes, we chose to use ZEUS-MP2 because of its supported features (e.g. spherical coordinates, non-ideal equations of state) and because its structure allows for the relatively easy addition of new features.

Our calculations are done in spherical coordinates, anticipating the evolution of the remnant to a quasi-spherical end state. In order to minimize the computational demands, we primarily perform 2.5D simulations, in which vector quantities can have a ϕ component, but its value does not vary along the ϕ direction. In general, we also assume reflection symmetry about $\theta = \pi/2$. In the Appendix, we briefly report additional calculations which confirmed the validity of these simplifications.

Our typical computational domain is characterized by the grid spacing in the r and θ directions and by the radius of the inner boundary. Unless otherwise specified, we adopt a logarithmic radial grid with $N_r = 64$ points per decade. The angular grid is uniform from $[0, \pi/2]$ with $N_\theta = 48$ angular zones. These values give a grid in which individual cells are roughly equal in radial and θ extent. We choose an inner radius such that only 0.1 per cent of the mass lies interior to that radius and then place the outer boundary at $10^4 r_{\text{inner}}$. We perform higher resolution simulations to confirm that our simulations are converged (see §A1).

We make several modifications to ZEUS-MP2 (based off of v2.12) in order to perform our calculations; we describe these modifications in the rest of this section.

2.1 Non-ideal Equation of State

We modify the code by the addition of the non-ideal Helmholtz equation of state (EoS), which provides an electron-positron EoS valid over a large range of physical conditions combined with the equations of state for an ideal gas of ions and for blackbody radiation (Timmes & Swesty 2000). With the addition of the EoS routines, one small algorithmic change is made: as suggested in Stone & Norman (1992), a predictor-corrector method is used to improve energy conservation during the calculation of the compressional heating term.

2.2 Shear Viscosity

In order to approximate the effects of magnetic stresses, we add shear stress terms to the hydrodynamic equations. That is, we are solving the equations

$$D_t \rho + \rho \partial_j v_j = 0 \quad (1)$$

$$\rho D_t v_i = -\partial_i P - \rho \partial_i \Phi + \partial_j T_{ij} \quad (2)$$

$$\rho D_t (e/\rho) = -P \partial_i v_i + T_{ij} T_{ij}/(\rho \nu) \quad (3)$$

where $D_t = \partial_t + v_i \partial_i$ is the convective derivative and we observe the usual Einstein summation conventions. The pres-

sure is denoted by P , and the mass and internal energy densities are represented by ρ and e respectively. The velocity vector is v_i . The anomalous stress tensor T_{ij} is defined as

$$T_{ij} = \rho\nu(\partial_i v_j + \partial_j v_i) \quad (4)$$

where ν is the dynamic viscosity.

A very similar modification of the ZEUS-2D code was made by Stone et al. (1999). We benefited from inspecting the source code that was used to perform the calculations reported in that work. We also used the results reported in Stone et al. (1999) as a reference against which to test our own implementation.

The viscous terms are evaluated using an operator split method and are updated during the source step (Stone & Norman 1992). To ensure numerical stability, the time step Δt must be chosen to be less than $\Delta t_{\text{visc}} \sim \min((\Delta r)^2/\nu)$, where the minimum is evaluated over the computational domain.

As a dimensionally motivated form for the dynamic viscosity coefficient, we adopt

$$\nu(r, \theta) = \alpha \frac{c_s^2(r, \theta)}{\Omega_k(r)} \quad (5)$$

where c_s is the local sound speed and Ω_k is the Keplerian angular velocity calculated using the mass enclosed at a given spherical radius. Portions of the merger remnant (see Fig. 1) are unstable to the magneto-rotational instability (MRI; Balbus & Hawley 1991) and the Tayler-Spruit dynamo (Tayler 1973; Spruit 2002). These processes may generate viscous stresses corresponding to α in the range $10^{-4} - 10^{-1}$; for order of magnitude estimates, see Shen et al. (2012). We adopt a fiducial value of $\alpha = 3 \times 10^{-2}$, though we confirm that the results of our calculations are not sensitive to this choice (see §A2).

As one moves to small r , (the origin being at the centre of the surviving WD; see §2.4), c_s and Ω_k approach constant values. We are using a logarithmic grid, so $\Delta r \propto r$ and therefore $\Delta t_{\text{visc}} \propto r^2$. The timestep constraint imposed by the Courant-Friedrichs-Lewy (CFL) condition depends linearly on Δr , so $\Delta t_{\text{CFL}} \propto r$. At sufficiently small radii, the viscous timestep becomes much less than the timestep required by the CFL condition. In practice, this occurs at a radius which is in our computational domain. In order to evolve the remnant over many viscous times, we apply the following *ad hoc* prescription. Within some radius r_ν we suppress the viscosity by a factor of $1/r$ such that the ratio of $t_{\text{visc}}/t_{\text{CFL}}$ remains constant. In order to make the cutoff smooth, the exact prescription is

$$\nu'(r, \theta) = \nu(r, \theta) \left(\frac{1}{1 + (r/r_\nu)^\beta} \right)^{1/\beta} \quad (6)$$

where $\beta = 4$ and r_ν is approximately the half-mass radius of the inner WD. As shown in the Appendix, we have verified that our results are insensitive to the details of this prescription. Physically, we would not expect the viscosity prescription in Equation 5 to hold as $r \rightarrow 0$ because this region within the WD is in approximate solid body rotation and is not MHD unstable.

Local numerical simulations of the MRI in accretion discs indicate that the azimuthal components of the stress-tensor, $T_{r\phi}$ and $T_{\theta\phi}$, are roughly a factor of 10 larger than the other components (e.g. Hawley et al. 1995; Stone et al. 1996).

Our default assumption then is to evolve with only these components in the stress tensor being non-zero. In §A3, we test the effect of including all components and find some quantitative, though not qualitative, differences between the two choices.

2.3 Nuclear Burning

In several of the model systems the temperatures reached are sufficiently high that the energy release from fusion is not negligible on the viscous time-scale. However, the conditions are not such that the local burning time-scale ever falls below Δt_{CFL} . Therefore, in order to minimize the computational load associated with calculating the burning, we implement an extremely simple 5 isotope nuclear network which is explicitly integrated at the hydrodynamic timestep. This captures the bulk of the energy release.

The 5 species we track are He, C, O, Ne, Mg (these are the 5 isotopes present in the initial compositions). These isotopes are connected by 4 processes, the triple- α process and α capture on each of C, O, and Ne. The rates of these processes were taken from the JINA REACLIB database (Cyburt et al. 2010). We neglect additional physics such as screening corrections because the burning primarily occurs at densities where such effects are unimportant. We refer to our own burning implementation as HeCONE.

As a test of both our own implementation and the assumptions that motivate it, we also coupled the 13 isotope α -chain network *aprox13* to the code (Timmes et al. 2000). The results were virtually identical, confirming the validity of our approach. See §A6 for quantitative comparisons of the results of these tests.

ZEUS-MP2 provides the ability to advect scalar quantities; we use this feature to track the mass fractions of the isotopes in our network. The algorithms do not guarantee the sum of the mass fractions remains equal to one after the advection step. Methods to restore this constraint in fluid codes have been reported in the literature (for example, Plewa & Müller 1999). However, for the sake of simplicity, immediately before evaluating the energy release from nuclear burning, we enforce the constraint $\sum X_i = 1$ by appropriately adjusting the mass fraction of the most abundant isotope.

2.4 Construction of Initial Conditions

Our starting point is the results of SPH simulations of double white dwarfs performed by Dan et al. (2011). The simulations were notable for their use of a more accurate initialization of the binary system at the onset of mass transfer than had been used in previous work. We calculate the viscous evolution of the merger remnants formed in each of their eight production runs, the parameters of which are summarized in Table 1. Throughout the rest of this paper, when we refer to “initial conditions,” this refers to the matter configurations at the end of these SPH simulations.

In order to map between the output of the SPH calculations and the staggered mesh of ZEUS-MP2 we adopt the following procedure. In SPH, the value of a quantity f at a

ID	M_2	M_1	M_{tot}	q	t_{end}	C_2	C_1
P1	0.2	0.8	1.0	0.25	95.0	He	CO
P2	0.3	1.1	1.4	0.27	62.0	He	CO
P3	0.5	1.2	1.7	0.42	35.0	He	ONeMg
P4	0.3	0.6	0.9	0.50	50.0	He	CO
P5	0.6	0.9	1.5	0.67	35.7	CO	CO
P6	0.2	0.3	0.5	0.67	30.0	He	He
P7	0.3	0.4	0.7	0.75	18.0	He	He
P8	0.9	1.2	2.1	0.75	30.0	CO	CO

Table 1. A summary of the systems simulated by Dan et al. (2011). ID is their run number. M_2 is the mass (in M_\odot) of the secondary, the less massive of the two WD; M_1 is the mass of the more massive primary. M_{tot} is the total mass of the system and $q = M_2/M_1$ is the mass ratio. t_{end} is the duration of the SPH simulation in terms of the initial orbital period. C_1 and C_2 are the compositions of the primary and the secondary WDs. See Table 1 in Dan et al. (2011) for more details.

position \vec{x} is given by

$$f(\vec{x}) = \sum_{i=1}^n \frac{m_i}{\rho_i} f_i W(|\vec{x} - \vec{x}_i|, h_i) \quad (7)$$

where W is the kernel function. The quantity of interest associated with the i -th SPH particle is denoted f_i . The SPH particle has mass, density, position and smoothing length m_i , ρ_i , \vec{x}_i and h_i respectively (e.g. Monaghan 1992). The sum runs over the total number of SPH particles, n .

Schematically, we construct our grid-based initial conditions by evaluating the five quantities that ZEUS-MP2 evolves (mass density ρ , internal energy density e and velocity \vec{v}) at each grid point. In our standard 2D simulations, we construct initial conditions that are explicitly invariant in the ϕ direction and are reflection-symmetric about $\theta = \pi/2$. Given these conditions, the total linear momentum of the remnant is guaranteed to be zero. Therefore, we choose the origin of our simulation coordinate system to be at the point of peak density, corresponding to the centre of the more massive (surviving) WD.

Explicitly, in order to calculate the value of a density (e or ρ) at a grid point with coordinates (r_i, θ_j) we evaluate

$$\rho_{ij} = \frac{1}{2N_\phi} \sum_{k=1}^{N_\phi} [\rho_{\text{SPH}}(r_i, \theta_j, \phi_k) + \rho_{\text{SPH}}(r_i, \pi - \theta_j, \phi_k)] \quad (8)$$

where N_ϕ is the number (typically $N_\phi = 32$) of equally-spaced points used to cover the interval $\phi \in [0, 2\pi)$. Now and throughout this section, the subscript SPH indicates a quantity extracted from the SPH simulation by the evaluation of Eq. 7.

Constructing the initial velocity vector requires slightly more complicated ϕ averaging. From the SPH data, we first construct the full velocity vector (with the components represented in Cartesian coordinates) at each of the grid locations where a component of the velocity will be defined. The staggered mesh employed by ZEUS-MP2 means that each velocity component is defined at a different spatial point (for details see Stone & Norman 1992). We take this into account, though we do not manifestly indicate it in the formulae below for the sake of compactness.

It is not simultaneously possible to conserve the kinetic energy of the fluid and its linear and angular momentum

when performing the ϕ -averaging. (This is simply a statement of the fact that in a non-uniform field, $\langle v^2 \rangle \neq \langle v \rangle^2$.) Given that we are interested in investigating the angular momentum evolution of the remnant, we choose to conserve momentum. In practice, the difference is relatively small; for the fiducial remnant, this averaging procedure changes the total kinetic energy by 1 per cent.

Therefore, to obtain the value of a component of the velocity \vec{v} , defined at a point (r_i, θ_j) we calculate

$$v_{ij} = \frac{1}{2N_\phi} \frac{1}{\rho_{ij}} \sum_{k=1}^{N_\phi} [\vec{p}_{\text{SPH}}(r_i, \theta_j, \phi_k) \cdot \hat{e}_{ij}(\phi_k) + \vec{p}_{\text{SPH}}(r_i, \pi - \theta_j, \phi_k) \cdot \hat{e}_{ij}(\phi_k)] \quad (9)$$

where \vec{p} is the momentum vector and \hat{e}_{ij} is the unit vector of the velocity component of interest at the point.

3 RESULTS

We expect that systems with similar mass ratios (q) and total masses (M_{tot}) will undergo similar evolution. Since the composition of a WD maps to a relatively well-defined mass range, we organize our discussion by the composition of the merging WDs. First, we discuss our fiducial 0.6+0.9 M_\odot CO+CO system. The outcomes of He+He, He+CO and He+ONeMg mergers are discussed on a more limited basis, emphasizing only the notable differences between these systems and our fiducial one. See Table 2 for a summary of the properties of our primary simulations. As shown in Table 1, Dan et al. (2011) label their simulations with a short identifier of the form Pn , where P represents production and n in an integer. For our own short IDs (shown in Table 2), we simply prepend Z (representing “ZEUS”) to the ID of the Dan et al. (2011) simulation that was used as the initial conditions.

In order to easily visualize our multi-D simulations, we will plot spherically averaged quantities against spherical radius. To calculate densities we perform a volume average, e.g.

$$\rho(r) = \frac{1}{2} \int_0^\pi d\theta \sin(\theta) \rho(r, \theta) \quad (10)$$

so that the appropriate quantity (e.g. mass) is conserved. To calculate other thermodynamic quantities such as temperature, we first calculate the spherically averaged mass and energy densities and then apply the equation of state. To calculate angular velocities, we restrict the average to a 45° wedge centred on the equator. As our simulations evolve toward a spherical end state, these 1D averages become an increasingly complete summary of the 2D structure of the remnant.

3.1 CO+CO systems

Our fiducial system (ZP5) is a super-Chandrasekhar CO+CO merger with $M_{\text{tot}} = 1.5M_\odot$ and $q = 2/3$. We simulate this system for 3×10^4 s, which is $\sim 5 \times 10^7$ timesteps of the hydrodynamics code. The simulation conserves mass to 1 part in 10^4 , energy to 0.5 per cent and angular momentum to one part in 10^3 . The evolution of an identical system was discussed in Shen et al. (2012), who performed a simple 1D

ID	$M_2 + M_1$	r_{inner} [cm]	Network	t_{end} [s]
ZP1	0.2 + 0.8	3.6×10^7	HeCONE	3.0×10^4
ZP2	0.3 + 1.1	2.2×10^7	HeCONE	3.0×10^4
ZP3	0.5 + 1.2	1.9×10^7	HeCONE	1.5×10^4
ZP4	0.3 + 0.6	4.4×10^7	HeCONE	4.0×10^4
ZP5*	0.6 + 0.9	2.9×10^7	None	3.0×10^4
ZP6	0.2 + 0.3	6.6×10^7	HeCONE	4.0×10^4
ZP7	0.3 + 0.4	5.7×10^7	HeCONE	4.0×10^4
ZP8†	0.9 + 1.2	1.9×10^7	aprox13	1.0×10^4

Table 2. Details of the viscous evolution calculations discussed in this paper. As an ID, we simply prepend Z (representing “ZEUS”) to the ID of the Dan et al. (2011) simulation that was used as the initial conditions. $M_2 + M_1$ is the mass of the secondary + primary in M_\odot . We will sometimes refer to systems by this sum. r_{inner} is the location of the inner boundary of our computational domain. Network indicates which nuclear network was used in the calculation. t_{end} is the end time of the simulation. All of the simulation parameters which were held fixed across all runs are discussed in the text. * fiducial model discussed in the most detail in the main text (in §3.1) † this simulation had a lower resolution, $N_r, N_\theta = 48, 32$.

calculation of the viscous evolution. Our multidimensional calculations confirm the schematic picture presented therein.

At the end of the SPH simulation, the primary white dwarf is relatively undisturbed and is surrounded by the remnants of the disrupted secondary. More than half of the disrupted material has primarily rotational support; the remainder was shock-heated in the merger and has thermal support. (A small amount $\sim 10^{-3} M_\odot$ is unbound in a tidal tail.) The merger remnant is in quasi-hydrostatic equilibrium, which we confirm by evolving these initial conditions without the action of viscous torques for many dynamical times, observing little change.

The black lines in Fig. 1 show the initial rotation profile. The primary WD is rotating rigidly; exterior to that is the disrupted secondary which is in Keplerian rotation. This hot, fully ionized material is unstable to magnetohydrodynamic instabilities such as the MRI. The turbulence generated by the saturation of the MRI leads to an enhanced viscosity and concomitant transport of angular momentum to larger radii (Balbus & Hawley 1991; Balbus 2003). As described in §2.2 we model this using an α -viscosity.

The viscosity also liberates energy present in the ϕ -velocity shear. Fig. 2 shows the evolution of the temperature and specific entropy profiles during the viscous evolution. Fig. 3 shows the final $\rho - T$ distribution and the evolution of the temperature peak in the $\rho - T$ plane during the viscous evolution. The viscous heating causes the peak temperature in the remnant to increase over the duration of the viscous phase by a factor of ~ 2 , to $\sim 8 \times 10^8$ K. The temperature peak is at a density of $\sim 5 \times 10^5 \text{ g cm}^{-3}$ and at those conditions the energy released from carbon burning exceeds neutrino losses and the burning becomes self-sustaining.

The carbon burning in our fiducial model is an unimportant energy source on the viscous time-scale, so the viscous evolution is not directly affected. However, the fact that carbon burning begins during the viscous evolution means that a convective carbon burning shell will develop in $\sim 10^6$ s. One consequence of this is that we expect the material exterior to the temperature peak at the end of the viscous evolu-

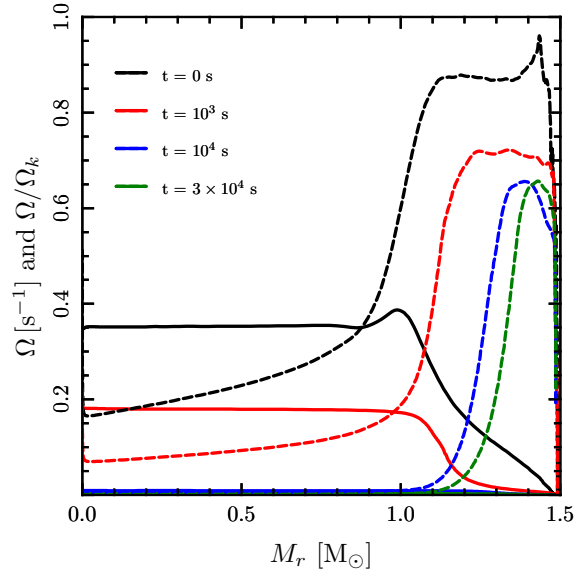


Figure 1. The evolution of the rotation profile of the fiducial $0.6+0.9 M_\odot$ CO+CO remnant. The solid lines are the angular velocity Ω and the dashed lines are its ratio to the Keplerian angular velocity, Ω/Ω_k . (The angular velocity is calculated using the material in a 45° wedge centred on the equator.) In the initial profiles (black), most of the material from the disrupted secondary ($M_r > 0.9$) is rotationally-supported with an angular velocity profile unstable to the MRI. The action of viscosity drives more of the remnant to solid body rotation and the accompanying heating leads to more of the remnant being thermally supported. We set $\alpha = 0.03$ for all the results in the main text. The Appendix shows that our results are nearly independent of α .

tion to quickly form a convective envelope. Future work will investigate the structure of this envelope, which is important for understanding the thermal evolution of the remnant and characterizing its observational properties.

One of the most striking results of our multi-D simulation is that the merger remnant evolves towards a final quasi-spherical steady state. (Given that there is rotation, the final state will actually be oblate, though in practice, the rotational velocities we find imply that it is quite spherical.) To quantify this, we define a simple “aspect ratio” as follows: draw an isodensity contour and take the ratio of the distance from the origin at the equator to that at the pole. As a rule of thumb, we find that the aspect ratio associated with a given radius approaches unity after about 10 viscous times have passed at that radius. The bottom panel of Fig. 4 shows this convergence clearly. The primary WD ends up with a thermally supported, nearly spherical envelope. The top panel of Fig. 4 shows the mass enclosed as a function of radius which illustrates how the outer thermally supported envelope expands to larger radii during the viscous evolution.

Our multi-dimensional simulations also allow us to capture processes like convection. We find that the viscous heating causes the remnant to evolve towards a convectively unstable state. Recently, García-Berro et al. (2012) discussed how convectively generated magnetic fields in merger remnants could potentially explain the origin of high-field WDs.

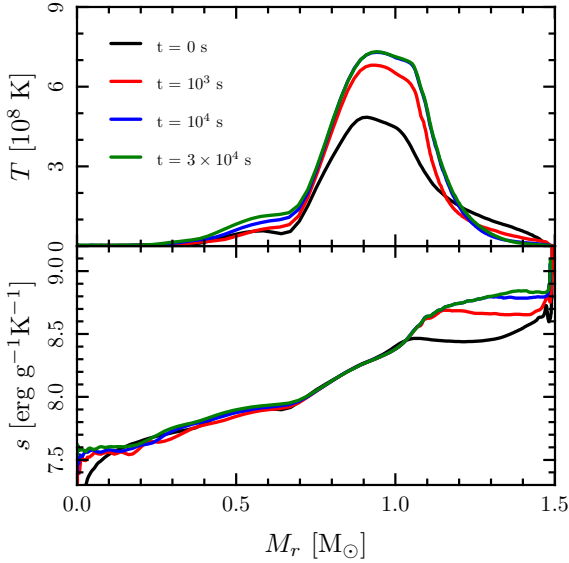


Figure 2. The evolution of the temperature (top) and specific entropy (bottom) profiles of the fiducial $0.6+0.9 M_{\odot}$ CO+CO remnant. Viscous heating increases the peak temperature by roughly a factor of two. Convection and viscous heating both contribute to the entropy evolution of the material from the disrupted secondary. As discussed in the text, these curves are 1D spherical averages of our 2D simulations.

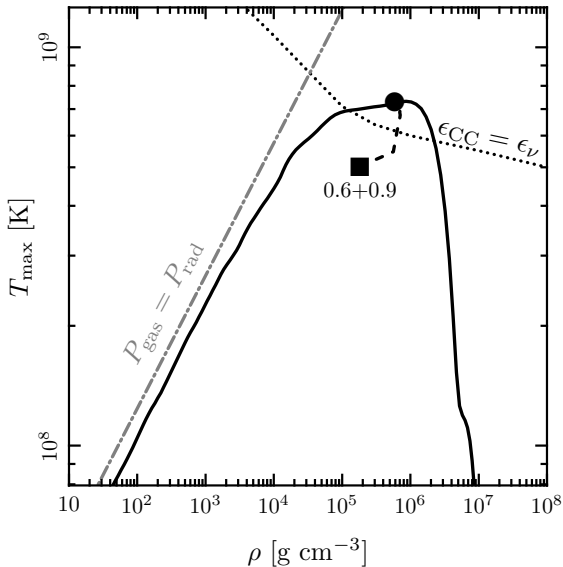


Figure 3. The evolution of the temperature peak in the $\rho - T$ plane. The dotted line indicates the break-even point where the energy release from carbon burning is equal to neutrino losses. The filled square (circle) is the peak temperature and corresponding density at the start (end) of the simulation, and the dashed line that connects them traces its evolution. The solid line is the full 1D $\rho - T$ profile of the quasi-spherical end state. The grey dash-dot line indicates where gas and radiation pressure are equal.

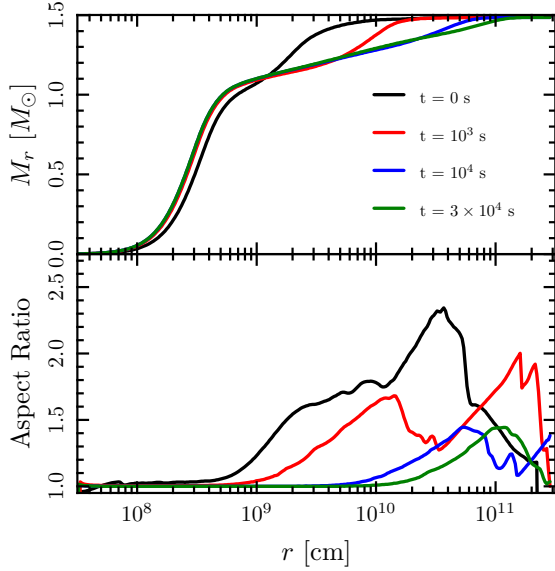


Figure 4. The evolution of the mass enclosed (top) as a function of spherical radius and the aspect ratio (bottom; see text for definition) for the fiducial $0.6+0.9 M_{\odot}$ CO+CO remnant. The convergence of the aspect ratio to a constant value ≈ 1 provides an indication that the end state has approximately been reached.

They noted that the conditions at the end of their own SPH simulations were unstable by the Schwarzschild criterion. However, given that this system has substantial rotational support and that we are evolving it in axisymmetry, a more appropriate test is the Høiland criterion. Our initial conditions are not unstable by the Høiland criterion and do not evolve towards an unstable state without the action of the viscous stresses.¹

Fig. 5 shows the 2D evolution of the fiducial system. In addition to the entropy and temperature, we plot two energy densities which are helpful in interpreting the evolution. One is the free energy available in the ϕ -velocity shear

$$\text{KE}_{\phi\text{-shear}} = \frac{1}{4} \rho \left(R \frac{d\Omega}{d \log R} \right)^2, \quad (11)$$

which shows the energy available for viscous heating. The other is the kinetic energy density in non-azimuthal motions

$$\text{KE}_{r,\theta} = \frac{1}{2} \rho (v_r^2 + v_\theta^2), \quad (12)$$

which is related to the kinetic energy associated with convective motions. Fig. 5 also plots isodensity contours, which emphasize the approach of the remnant to a spherical state.

Given previous work on viscous, geometrically thick accretion flows, one might expect that material would outflow along the poles during the viscous evolution. When the viscous time is much less than the cooling time and the mass inflow is assumed to be conservative (that is, mass does not leave the system), the transport of energy and the release of gravitational potential energy are such that

¹ The physical initial conditions are of course unstable in MHD, as it is the MRI that is giving rise to the effective viscosity.

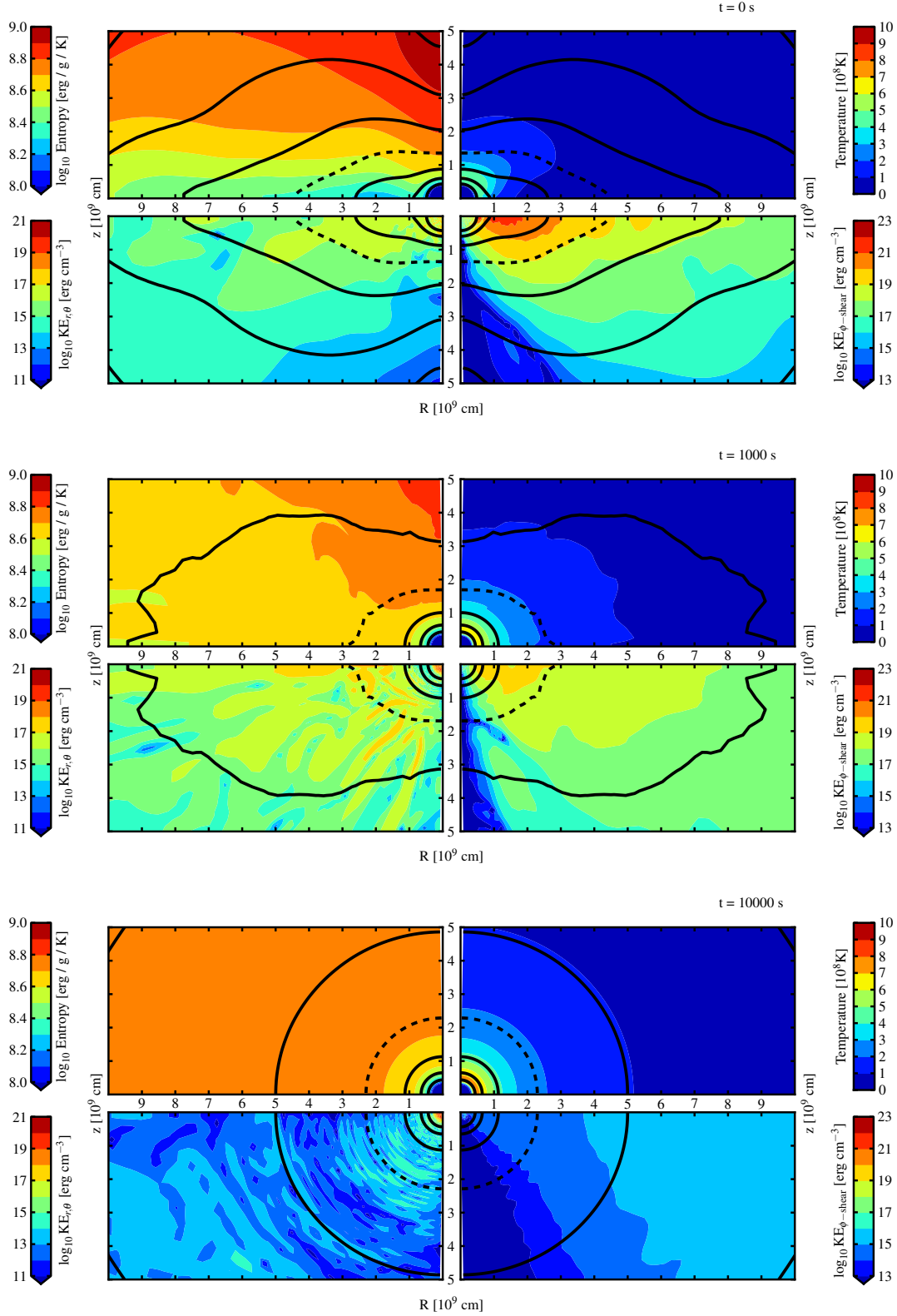


Figure 5. A visual overview of the 2D evolution of the fiducial $0.6+0.9 M_{\odot}$ CO+CO merger remnant. Within each panel, the top two subpanels are thermodynamic quantities (s, T) and the bottom two subpanels are kinetic energy densities (non-azimuthal, ϕ -shear). The black contours are density, spaced one per decade. The dashed contour is $\rho = 10^3 \text{ g cm}^{-3}$. The main panels are snapshots of the simulation at the indicated times. *Top Panel:* The initial conditions, note the large “free” energy apparent in the shearing, Keplerian disc. *Middle Panel:* The action of viscosity has dissipated some of the shear and heated the material. The remnant has become convectively unstable as can be seen in the striation of the non-azimuthal KE. *Bottom Panel:* The remnant has settled down into a quasi-spherical steady state.

material has a positive Bernoulli parameter (Be) (Narayan & Yi 1994; Blandford & Begelman 1999). Therefore, solutions in which the mass flow is not conservative may be more physical. Non-radiative accretion flows are also predicted to be convectively unstable. Models based on these ideas (e.g Blandford & Begelman 2004) developed solutions with prominent outflows. Hydrodynamic numerical simulations such as those by Stone et al. (1999) exhibited the slow outflow of marginally bound material in the polar direction. MHD simulations such as those by Stone & Pringle (2001) found somewhat more prominent outflows than in the hydrodynamic simulations.

We do not observe outflows in our simulations. Fig. 6 shows the fraction of mass on our grid with positive Be $\equiv f_{\text{Be}>0}$. Initially $f_{\text{Be}>0} \sim 3 \times 10^{-3}$, corresponding to the unbound material in the tidal tail. This material flows out of the outflow boundary and afterwards there is little unbound mass ($f_{\text{Be}>0} \sim 10^{-5}$). In order to isolate the effects of viscosity on the unbound material, we ran a simulation without the viscosity and calculated $f_{\text{Be}>0}$ (dotted blue line). The orange line in Fig. 6 shows the integrated difference in the mass that flowed through the outer boundary with Be > 0 in simulations with and without viscosity. This difference is very small $< 10^{-5} M_{\odot}$. We do not claim that this specific value is robust, but the conclusion that the viscous evolution of WD merger remnants unbinds a only a very small amount of mass appears to be.

The initial conditions of our simulations are rather different than the initial conditions of most radiatively inefficient accretion simulations. Such simulations typically allow the material to move through several orders of magnitude in radius before reaching an inflow boundary representing a black hole. By contrast, the radial dynamic range between the surface of the primary WD and the bulk of the material in the initial rotationally-supported disc is small, a factor of ~ 5 . The presence of a “hard surface” (the primary WD) means that as material accretes, the radius where material is pressure-supported moves outward, further suppressing the dynamic range between the effective inner boundary and the disc.

In order to understand the results of our WD merger remnant simulations in the context of accretion tori simulations, we generate accretion tori like those in Stone et al. (1999) and adjusted the inner boundary condition (reflecting vs. inflow) and the dynamic range between the initial torus and the inner boundary. We run the simulations for several orbits and calculate the resulting amount of unbound material $f_{\text{Be}>0}$. At a radial dynamic range between the initial torus and the inner boundary of 100 and with an inflow boundary, we find $f_{\text{Be}>0} \sim 4 \times 10^{-2}$, much larger than in our WD merger remnant calculations (see Fig. 6). Decreasing the dynamic range to 10 results in $f_{\text{Be}>0} \sim 4 \times 10^{-3}$. At this dynamic range, changing the inner boundary condition to reflecting causes $f_{\text{Be}>0}$ to peak $\sim 10^{-4}$ and then fall as the simulation continues. These results support our conclusion that only a very small amount of mass is unbound during the viscous evolution of WD merger remnants ($f_{\text{Be}>0} \lesssim 10^{-5}$).

In addition to our fiducial $0.6+0.9 M_{\odot}$ CO+CO system, we also simulate a very super-Chandra $0.9+1.2 M_{\odot}$ system (ZP8). This system quickly starts C+C burning, although the burning does not become dynamical (see Section 4.2). While the energy release from the burning on the vis-

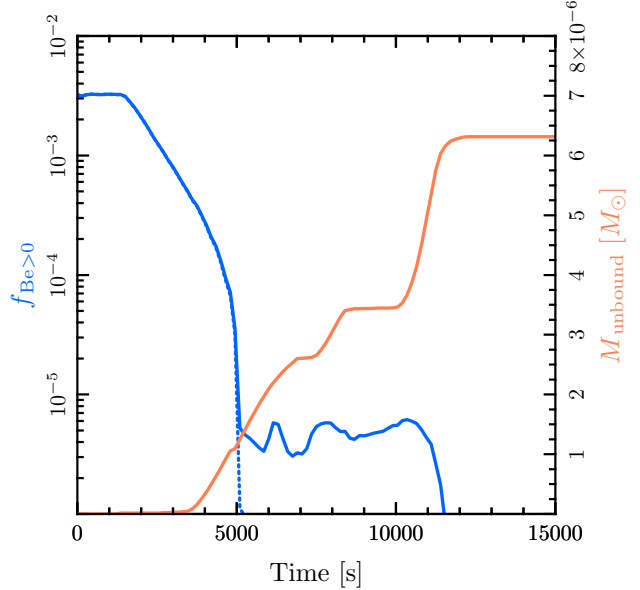


Figure 6. Viscously unbound material. The left (blue) scale indicates the fraction of mass with positive Bernoulli constant at a given time in the evolution of the fiducial $0.6+0.9 M_{\odot}$ CO+CO merger remnant. The dominant contribution is the tidal tail; the large decrease in $f_{\text{Be}>0}$ over the first 5000 s is this material flowing out of the simulation domain. The solid (dotted) line is the mass fraction with Be > 0 in a simulation with (without) viscosity. The right (orange) scale is the integrated amount of mass that has flowed out of the simulation domain with positive Be due to the influence of viscosity. This is the integrated difference between the two blue curves. Little additional material ($\leq 10^{-5} M_{\odot}$) is unbound by the viscous evolution.

cous time is locally non-negligible, the mass outflow is not affected by the presence of nuclear energy generation. As shown in the Appendix, the energy release is not significant enough to affect the global behavior of the remnant.

3.2 He+He systems

The evolution of He+He merger remnants is broadly similar to our fiducial CO+CO case. The larger size and lower mass of the He WDs mean that the temperatures reached at the end of the SPH calculations are not as high. However, these temperatures are still high enough that we elect to track the energy release from He burning in our simulations. We do this using the simple nuclear network described in Section 2.3.

Fig. 7 shows the evolution of the temperature and rotation rate for a $0.2+0.3 M_{\odot}$ system (ZP6). This has the same mass ratio $q = 2/3$ as the fiducial system, but with a total mass 3 times lower. The initial temperature and rotation profiles look qualitatively similar to our fiducial system. Appropriately scaling these values by the total mass, they are even quantitatively similar. However, the final state appears somewhat different, most conspicuously because of the narrow temperature peak that forms at an enclosed mass of $\sim 0.38 M_{\odot}$.

This qualitative difference in evolution is most clear in Fig. 8, which shows the evolution of the temperature maxi-

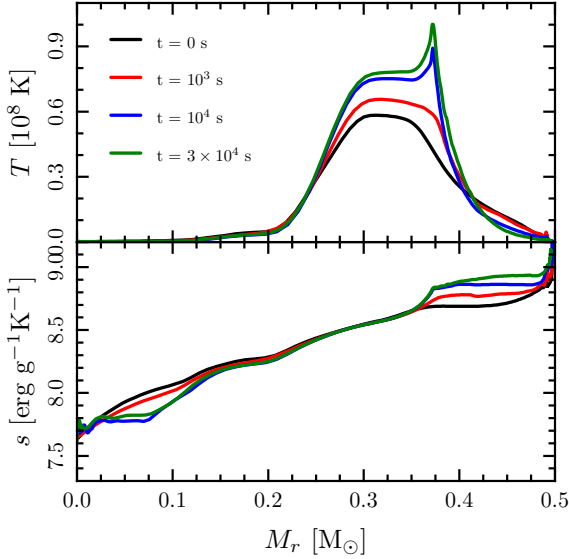


Figure 7. A 1D summary of the $0.2+0.3 M_{\odot}$ He+He remnant evolution. The temperature (top panel) and rotation (bottom panel) profile at beginning, intermediate and final times. The temperature evolution appears qualitatively different than our fiducial model; as explained in the text, this is due to this lower mass remnant remaining gas pressure dominated. The rotation evolution is qualitatively the same as the fiducial model.

mum and the corresponding density. The temperature maximum evolves to lower density during the viscous phase, unlike in CO+CO mergers where it evolves to higher density (see Fig. 3). This effect is unrelated to the presence of fusion, as the time-scale for burning is still relatively long. This difference in evolution is also not a qualitative difference in the merger outcome or the viscous evolution, but rather is due to the different contribution of gas and radiation pressure in the merger remnants. The grey dash-dot line in Figs. 3 and 8 shows where $P_{\text{gas}} = P_{\text{rad}}$. The He+He case remains gas pressure dominated, so the location of the peak temperature corresponds to the location of the viscous heating. Lower densities, which are at larger radii and have corresponding longer viscous time-scales, are heated at later times. In the CO+CO case, radiation pressure has a larger relative contribution initially and once material has been heated such that radiation pressure begins to become important, additional heating is no longer as effective in raising the temperature. Therefore, larger relative increases in T occur at higher densities where gas pressure continues to dominate, and thus the peak T moves to higher densities.

3.3 He+CO systems

In the He+CO systems, the primary is more massive and hence more compact than in the He+He mergers. This leads to higher temperatures during the merger. The lower temperatures required for He burning (versus C burning) mean that the effects of nuclear burning are more pronounced in these systems. Fig. 9 shows the evolution of the temperature peak in these simulations.

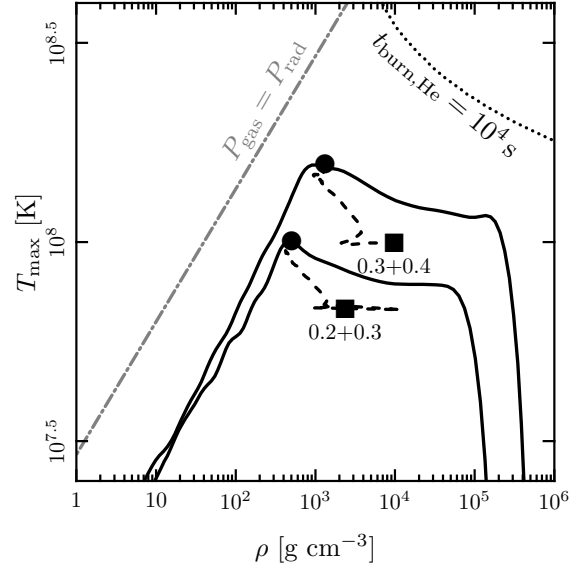


Figure 8. The evolution of the temperature peak for the He+He merger remnants. The dotted line labeled $t_{\text{burn,He}} = 10^4$ s indicates the region where the time-scale for energy release by He fusion is equal to the time-scale of the simulation. The filled square (circle) is the peak temperature and corresponding density at the start (end) of the simulation, and the dashed line that connects them traces its evolution. The solid line is the full 1D $\rho-T$ profile of the quasi-spherical end state. The grey dash-dot line indicates where gas and radiation pressure are equal.

The $0.3+0.6 M_{\odot}$ He+CO system (ZP4) is the only one of the systems we simulate in which the final state deviates significantly from approximate spherical symmetry. The remnant itself is spherical, but at the interface between the material from the He and CO WDs the composition varies between the equator and pole. This explains why the final peak temperature does not lie on the final spherically-averaged $\rho-T$ profile shown in Fig. 9. This system has the highest mass ratio of any mixed composition system we simulated and at higher mass ratios the secondary more strongly affects the primary. However, because the efficiency of mixing likely depends on dimensionality and angular momentum transport (α -viscosity vs MHD), we do not expect our work to provide a robust prediction of the details of such mixing.

3.4 He+ONeMg

One system in our study is composed of a $0.5 M_{\odot}$ He WD and a $1.2 M_{\odot}$ ONeMg WD. Its evolution is very similar to the systems previously discussed. Notably, the high primary WD mass means that the He (from the secondary) reaches quite high temperatures. The burning time in this system is thus quite short, less than the viscous time, though not less than the dynamical time (see §4.2).

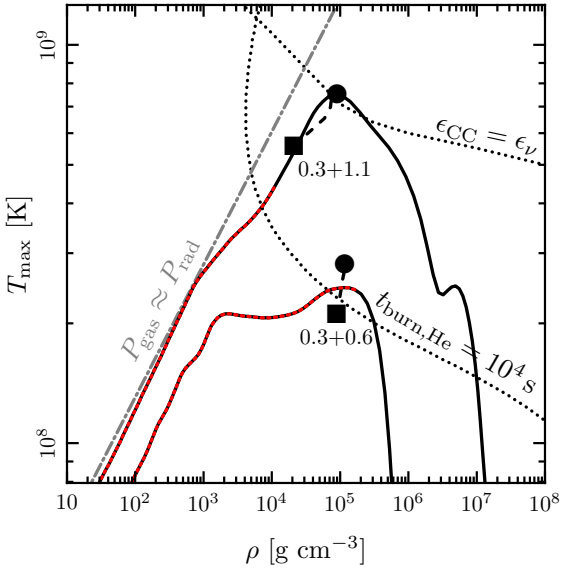


Figure 9. The evolution of the temperature peak for the He+CO remnants. The dotted line labeled $\epsilon_{CC} = \epsilon_\nu$ indicates the break-even point where the energy release from carbon burning is equal to neutrino losses. The dotted line labeled $t_{\text{burn,He}} = 10^4$ s indicates the region where the time-scale for energy release by He fusion is equal to the time-scale of the simulation. The filled square (circle) is the peak temperature and corresponding density at the start (end) of the simulation, and the dashed line that connects them traces its evolution. The solid line is the full 1D $\rho - T$ profile of the quasi-spherical end state. The red dotted section shows where the helium mass fraction exceeds 50 per cent. The grey dash-dot line indicates where gas and radiation pressure are equal. The peak temperature in the 0.3+0.6 $\rho - T$ profile does not correspond to the final peak temperature indicated by the solid circle. At the spherical radius of the temperature peak, the chemical composition varies from pole to equator and hence the averaged temperature at that point is not equal to the 2D peak.

4 DISCUSSION

4.1 Fitting Formulas

The end states of our simulations will be useful as a starting point for future work concerning the thermal evolution of WD merger remnants. To aid such work, we provide fitting formulae that allow one to easily construct a physical state which is in rough quantitative agreement with our results.

The 1D profiles we extract at the end of our calculations have the following schematic form. At the centre is a core of cold, degenerate material. This is surrounded by a hot envelope, the outer portion of which was convective and so has an entropy that is roughly spatially constant.

This picture allows a simple, *post hoc* model of the end state of our simulations. We write down a piecewise equation of state in which there is a central mass (M_c) described by a zero-temperature equation of state. This is surrounded by an isothermal region corresponding to the temperature peak which has mass M_{tp} . The rest of the external material has a polytropic equation of state. Empirically the polytropic index of $n = 3$ provides a good fit to all of our simulations. For systems at high temperatures, such as our 0.3+1.1 M_\odot

ID	ρ_c [g cm $^{-3}$]	M_c	M_{tp}
ZP1 [†]	8.8×10^6	0.71	0.10
ZP2 [†]	4.7×10^7	0.98	0.12
ZP3 [†]	9.5×10^7	1.05	0.16
ZP4 [†]	3.8×10^6	0.53	0.13
ZP5	2.8×10^7	0.84	0.20
ZP6	6.4×10^5	0.28	0.08
ZP7	1.5×10^6	0.38	0.12
ZP8	3.3×10^8	1.11	0.24

Table 3. The parameters from our fits (see Equations 13-15 and surrounding discussion). ID is the run ID. ρ_c is the central density extracted from the end of our simulations. M_c is the amount of mass (in M_\odot) in the zero-temperature degenerate core. M_{tp} is the amount of mass (in M_\odot) in the isothermal region, loosely corresponding to the temperature peak. [†]marks those systems which have a mixed chemical composition.

He+CO merger, this is unsurprising as the material in the convective region is nearly radiation dominated, implying an adiabatic index near $\gamma = 4/3$. For systems such as low total mass He+He mergers (ZP6 & ZP7), the matter is gas pressure dominated, which would imply an adiabatic index of 5/3. However these systems have larger residual entropy gradients, such that the relationship $P \propto \rho^{4/3}$ roughly holds. Since we can provide satisfactory fits without introducing an additional parameter, we choose $n = 3$ for all our fits.

Quantitatively

$$P(\rho) = \begin{cases} P_{\text{ZT}}(\rho) & \text{if } M_r < M_c \\ K_1 \rho & \text{if } M_c < M_r < M_c + M_{\text{tp}} \\ K_2 \rho^{1+1/n} & \text{if } M_c + M_{\text{tp}} < M_r \end{cases} \quad (13)$$

where P_{ZT} is the pressure of a zero temperature Fermi gas with $\mu_e = 2$ (e.g Shapiro & Teukolsky 1983). K_1 and K_2 are set by the condition that ρ , P are continuous at the transitions between regimes.

In combination with the equations of hydrostatic equilibrium and mass conservation in 1D spherical coordinates

$$\frac{dM_r}{dr} = 4\pi r^2 \rho \quad (14)$$

$$\frac{dP}{dr} = -\frac{GM_r \rho}{r^2} \quad (15)$$

and a central boundary condition $\rho(r_{\text{inner}}) = \rho_c$, this is sufficient to fully specify a 1D model. We set ρ_c to be the value of the central density at the end of our simulations.

For each of our simulations we fit for the two masses M_c and M_{tp} . Table 3 reports the results of these fits. Fig. 10 shows the results of the fit to our fiducial model. The fit reproduces the observed quantities to within ~ 30 per cent. The fit is worst in the region described by the isothermal equation of state, which is unsurprising since this is the least physically motivated part of our effective equation of state.

Our fitting procedure does not use or provide any spatial information about the chemical composition. As a rough approximation, one can simply retain the initial Lagrangian composition of the system with the secondary outside of the primary. In the mergers where the chemical compositions of the WDs were initially identical, this is a good approximation because nuclear reactions do not significantly alter the composition (for the set of mergers we considered). For mergers where the WDs had different compositions (which

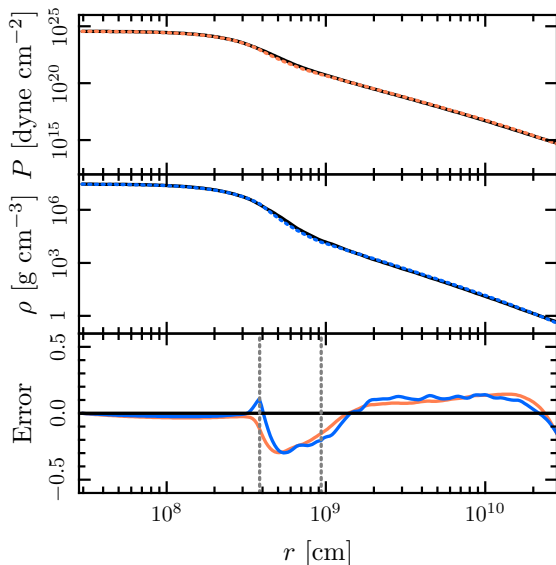


Figure 10. The simple two-parameter fit to the fiducial $0.6+0.9 M_{\odot}$ CO+CO merger remnant (see Equations 13-15 and surrounding discussion). The upper two panels show the pressure and density profiles from the simulation as solid lines. The fits are shown as dashed lines. The bottom panel shows the relative error between the fit and the simulation. The vertical grey lines show the position of the transitions in the piecewise equation of state.

are marked in Table 3), the assumption that the composition is conserved in a Lagrangian sense is substantially more crude because of mixing and the effects of nuclear burning. In those cases, these simple fits would be inappropriate for work in which inaccuracies in the chemical composition could have a large effect.

4.2 Burning Time

Recently there has been considerable interest in the possibility of central carbon detonations triggered by the detonation of a helium layer on the surface of a CO WD. During a WD merger, conditions for detonations may be reached in instabilities in the accretion stream (Guillochon et al. 2010) or at surface contact (e.g. Dan et al. 2012). The systems we consider did not reach detonation conditions during the SPH simulations (though those could not resolve accretion stream instabilities).

During the phase of evolution that we simulate, viscous heating does increase the temperature and either initiate or increase the rate of burning. Fig. 11 shows the minimum burning times and corresponding temperatures for the eight systems we simulate. We calculate the minimum nuclear burning time as $t_{\text{burn}} = c_P T / \epsilon_{\text{nuc}}$, where c_P is the specific heat at constant pressure, T is the temperature and ϵ_{nuc} is the specific energy generation rate from nuclear reactions.

The minimum burning time is not necessarily located at the location of peak temperature, as differences in the chemical composition (for example, the presence of helium) may make the rate of energy release greater at a different location. In general, the viscous heating causes a monotonic

increase in the temperature. Therefore, initially the burning time drops. Then, in cases where the burning time is less than the viscous time, changes in the composition (such as the depletion of helium) begin to shift the minimum burning time to slightly lower temperatures where more material remains to burn.

In the case of the $0.5+1.2 M_{\odot}$ merger, the burning time, which is $\sim 40 t_{\text{dyn}}$ at the beginning of the simulation, decreases to as low as $\sim 2 t_{\text{dyn}}$, where the dynamical time is calculated as $t_{\text{dyn}} = P / (\rho g c_s)$. The ratio $t_{\text{burn}} / t_{\text{dyn}} \lesssim 1$ provides a rough criterion for possible detonation. Detailed conditions for detonations are still a topic of current research and almost certainly require resolving smaller length scales than our current simulations can do (for example, see discussion in §3.2 of Woosley & Kasen 2011).

Using the value of $t_{\text{burn}} / t_{\text{dyn}}$ as a guide, viscous heating does not cause any of the remnants that we simulated to experience dynamical burning. However, with the low value of $t_{\text{burn}} / t_{\text{dyn}}$ for the $0.5+1.2 M_{\odot}$ system and the temperature sensitivity of nuclear reactions, we expect that systems only slightly more massive would experience dynamical burning. Furthermore, if there are stochastic fluctuations, it is even possible that this particular system could experience dynamical burning. Several figures in Dan et al. (2012) draw contours of $t_{\text{burn}} / t_{\text{dyn}}$ in the space of primary/secondary WD mass. For systems where the merger has brought the system close to the critical value of $t_{\text{burn}} / t_{\text{dyn}}$, we anticipate that viscous evolution would cause this value to fall below 1. Viscous evolution reduces $t_{\text{burn}} / t_{\text{dyn}}$ by a factor of ~ 20 in run ZP3, so we speculate that dynamical burning might occur for those systems with $1 \lesssim t_{\text{burn}} / t_{\text{dyn}} \lesssim 10$ in figure 8 of Dan et al. (2012). Future work will quantitatively address this question by simulating a wider range of merger remnants.

5 CONCLUSIONS

The merger remnants of binary white dwarfs are differentially rotating and unstable to MHD instabilities like the MRI. As outlined by Shen et al. (2012), MHD stresses give rise to a viscous phase of evolution which occurs on a time-scale much less than the thermal time. To investigate the outcome of this viscous evolution, we perform multi-dimensional hydrodynamic calculations of the evolution of WD binary remnants under the action of an α -viscosity. The initial conditions for these calculations are the SPH simulations by Dan et al. (2011). We find that these remnants evolve towards spherical states on time-scales of hours. This confirms the arguments in Shen et al. (2012) that the post-merger evolution of WD merger remnants is via viscous redistribution of angular momentum that leads to nearly solid body rotation. The transport of angular momentum outwards removes rotational support from the majority of the mass leading to a nearly spherical remnant. *The dynamics during this phase is not consistent with accretion at the Edington limit*, as in previous models of WD merger remnants (e.g. Nomoto & Iben 1985; Saio & Nomoto 1998, 2004; Pieranti et al. 2003b,a). Instead, the viscous evolution of WD merger remnants is much more analogous to that of a differentially rotating star.

Viscous heating associated with the approach to solid

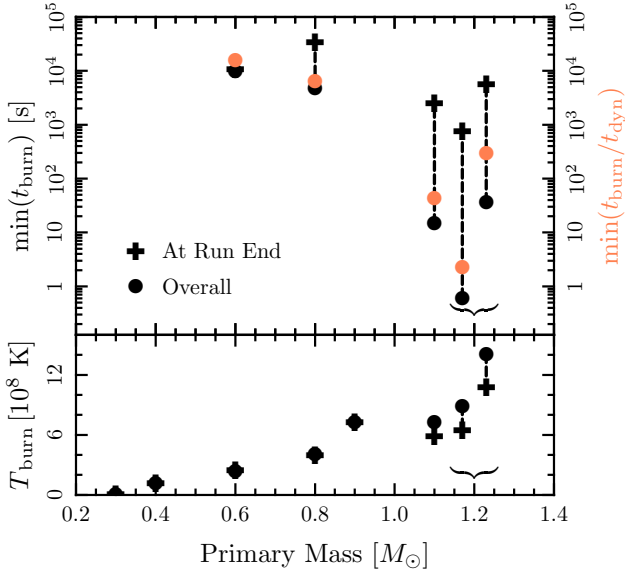


Figure 11. The shortest burning time (top panel) and corresponding temperature (bottom panel) for each of our simulated systems. The x-axis is the mass of the primary WD. Two systems have the same primary mass of $1.2 M_{\odot}$ and are slightly offset on the x-axis for visual clarity (ZP3 to the left and ZP8 to the right). In the top panel, the circle represents the shortest burning time reached overall, that is at any point during the simulation; the cross represents the burning time at the end of the simulation. They are connected by a dashed line to guide the eye and indicate that intermediate values are achieved. The same symbols in the bottom panel show the temperatures at the corresponding locations. Because of varying chemical composition, the temperature associated with the shortest burning time is not necessarily the global peak temperature. The right axis of the top panel and the orange circles show the ratio $t_{\text{burn}}/t_{\text{dyn}}$ (as defined in the text) at conditions corresponding to the black circles. In no case does the burning time ever reach the dynamical time, though in ZP3 it is within a factor of two.

body rotation unbinds only a very small amount of mass ($\lesssim 10^{-5} M_{\odot}$ in our fiducial calculation). This is in contrast to some of the intuition developed in the context of radiatively inefficient accretion flows, which predict outflows. To understand this, we perform simple accretion tori calculations which indicate that the relatively small radius difference between the disc and the surface of the WD can explain why only a small amount of mass becomes unbound (see §3.1).

Viscous heating causes one of the systems we simulate to reach conditions of nearly dynamical He burning, so it is possible that the post-merger viscous evolution triggers a detonation in some cases. Recently Dan et al. (2012) presented a suite of more than 200 WD merger simulations which more thoroughly populate the q - M_{tot} plane. They found that many of these systems reached the conditions for detonation during the merger (see for example their figures 6 & 8). In our calculations, $\min(t_{\text{burn}}/t_{\text{dyn}})$ decreases by a factor of ~ 10 during the viscous phase (see §4.2). As a result, we speculate that systems that reach $t_{\text{burn}}/t_{\text{dyn}} \lesssim 10$ during the merger may reach conditions for detonation during the subsequent viscous phase. Such a system is not among

those that we simulate (though run ZP3 was close). It is thus likely that heating during the post-merger viscous evolution significantly increases the region of parameter space in which one expects explosive burning during WD mergers, which could increase the rates of Type Ia or .Ia supernovae (Bildsten et al. 2007) associated with WD mergers.

Our purely hydrodynamic simulations cannot address the effects of magnetic fields. MHD simulations resolving the action of the MRI would allow a more realistic treatment of the viscous stresses than an α -viscosity², though the quantitative insensitivity of our results to the value of α leads us to think that our conclusions are robust. Converting our fiducial value of α to a magnetic field strength gives $|B| \sim \sqrt{4\pi\alpha\rho c_s^2} \sim 10^{10} \text{ G}$. The implications of this estimate for the subsequent evolution of the merger remnant depend on the structure of the field. The generation of a large-scale field could lead to the formation of a strongly magnetized WD, which would be rapidly rotating and would quickly spin down via a magnetized wind. The presence of a strong magnetic field would also affect the conduction of heat in the interior of the WD. Alternatively, it is possible that the strong field is relatively small scale and so efficiently redistributes angular momentum in the interior of the remnant but does not significantly affect its global properties.

The end states of our calculations provide a starting point for investigations of the long-term thermal evolution of WD merger remnants. In our fiducial case, we expect that the luminosity from the nuclear burning will drive convection, establishing an extended convective envelope with its base at slightly larger radii than the temperature peak. The object will likely grow to have a radius comparable to that of a giant star and correspondingly a relatively cool effective temperature like the models presented in Shen et al. (2012). There are clear opportunities for future work in the self-consistent thermal evolution of these objects and their consequences for Type Ia supernovae, neutron stars, R Coronae Borealis stars and other phenomena.

ACKNOWLEDGMENTS

We thank Frank Timmes for making the Helmholtz equation of state and the aprox13 reaction network publicly available and for a helpful email exchange related to their use. We thank Sterl Phinney, Lars Bildsten, Brian Metzger and Dan Kasen for useful conversations. JS thanks Prateek Sharma for helpful discussions about the ZEUS code. The 2D calculations were performed on Henyey, which is supported by NSF AST Grant 0905801. We thank Dan Kasen for providing computational time for our 3D calculations. This research used resources of the National Energy Research Scientific Computing Center, which is supported by the Office of Science of the U.S. Department of Energy under Contract No. DE-AC02-05CH11231. JS is supported by an NSF

² It is worth noting that MHD simulations which capture the evolution of the entire remnant promise to be quite challenging. The instabilities in regions where $d\Omega/dr > 0$ are likely to be short wavelength non-axisymmetric modes that have a different time-scale and spatial scale than the MRI modes that operate where $d\Omega/dr < 0$. Correctly capturing the physics both inside and outside the rotation peak will be extremely difficult.

Graduate Research Fellowship. EQ & JS are also supported in part by the David and Lucile Packard Foundation and the Thomas and Alison Schneider Chair in Physics. KJS is supported by NASA through Einstein Postdoctoral Fellowship grant number PF1-120088 awarded by the Chandra X-ray Center, which is operated by the Smithsonian Astrophysical Observatory for NASA under contract NAS8-03060. MD and SR are supported by Deutsche Forschungsgemeinschaft under grants RO-3399/4-1 and RO-3399/4-2. This research has made use of NASA's ADS Bibliographic Services.

REFERENCES

Balbus S. A., 2003, *ARA&A*, 41, 555
 Balbus S. A., Hawley J. F., 1991, *ApJ*, 376, 214
 Benz W., Cameron A. G. W., Press W. H., Bowers R. L., 1990, *ApJ*, 348, 647
 Bildsten L., Shen K. J., Weinberg N. N., Nelemans G., 2007, *ApJ*, 662, L95
 Blandford R. D., Begelman M. C., 1999, *MNRAS*, 303, L1
 Blandford R. D., Begelman M. C., 2004, *MNRAS*, 349, 68
 Bloom J. S., Kasen D., Shen K. J., Nugent P. E., Butler N. R., Graham M. L., Howell D. A., Kolb U., Holmes S., Haswell C. A., Burwitz V., Rodriguez J., Sullivan M., 2012, *ApJ*, 744, L17
 Brown W. R., Kilic M., Allende Prieto C., Kenyon S. J., 2010, *ApJ*, 723, 1072
 Clayton G. C., Geballe T. R., Herwig F., Fryer C., Asplund M., 2007, *ApJ*, 662, 1220
 Cyburt R. H., Anthor A. M., Ferguson R., Meisel Z., Smith K., Warren S., Heger A., Hoffman R. D., Rauscher T., Sakharuk A., Schatz H., Thielemann F. K., Wiescher M., 2010, *ApJS*, 189, 240
 Dan M., Rosswog S., Guillochon J., Ramirez-Ruiz E., 2011, *ApJ*, 737, 89
 Dan M., Rosswog S., Guillochon J., Ramirez-Ruiz E., 2012, *MNRAS*, 422, 2417
 Fuller J., Lai D., 2012, *MNRAS*, 421, 426
 García-Berro E., Lorén-Aguilar P., Aznar-Siguán G., Torres S., Camacho J., Althaus L. G., Córscico A. H., Külebi B., Isern J., 2012, *ApJ*, 749, 25
 Guillochon J., Dan M., Ramirez-Ruiz E., Rosswog S., 2010, *ApJ*, 709, L64
 Hawley J. F., Gammie C. F., Balbus S. A., 1995, *ApJ*, 440, 742
 Hayes J. C., Norman M. L., Fiedler R. A., Bordner J. O., Li P. S., Clark S. E., ud-Doula A., Mac Low M.-M., 2006, *ApJS*, 165, 188
 Iben Jr. I., Tutukov A. V., 1984, *ApJS*, 54, 335
 Kilic M., Brown W. R., Allende Prieto C., Kenyon S. J., Heinke C. O., Agüeros M. A., Kleinman S. J., 2012, *ApJ*, 751, 141
 Marsh T. R., Nelemans G., Steeghs D., 2004, *MNRAS*, 350, 113
 Monaghan J. J., 1992, *ARA&A*, 30, 543
 Mullally F., Badenes C., Thompson S. E., Lupton R., 2009, *ApJ*, 707, L51
 Narayan R., Yi I., 1994, *ApJ*, 428, L13
 Nelemans G., 2009, *Classical and Quantum Gravity*, 26, 094030
 Nomoto K., Iben Jr. I., 1985, *ApJ*, 297, 531

Pakmor R., Kromer M., Röpke F. K., Sim S. A., Ruiter A. J., Hillebrandt W., 2010, *Nature*, 463, 61
 Pakmor R., Kromer M., Taubenberger S., Sim S. A., Röpke F. K., Hillebrandt W., 2012, *ApJ*, 747, L10
 Piersanti L., Gagliardi S., Iben Jr. I., Tornambé A., 2003a, *ApJ*, 598, 1229
 Piersanti L., Gagliardi S., Iben Jr. I., Tornambé A., 2003b, *ApJ*, 583, 885
 Plewa T., Müller E., 1999, *A&A*, 342, 179
 Raskin C., Scannapieco E., Fryer C., Rockefeller G., Timmes F. X., 2012, *ApJ*, 746, 62
 Saio H., Jeffery C. S., 2000, *MNRAS*, 313, 671
 Saio H., Nomoto K., 1985, *A&A*, 150, L21
 Saio H., Nomoto K., 1998, *ApJ*, 500, 388
 Saio H., Nomoto K., 2004, *ApJ*, 615, 444
 Schaefer B. E., Pagnotta A., 2012, *Nature*, 481, 164
 Shapiro S. L., Teukolsky S. A., 1983, *Black holes, white dwarfs, and neutron stars: The physics of compact objects*
 Shen K. J., Bildsten L., Kasen D., Quataert E., 2012, *ApJ*, 748, 35
 Spruit H. C., 2002, *A&A*, 381, 923
 Stone J. M., Hawley J. F., Gammie C. F., Balbus S. A., 1996, *ApJ*, 463, 656
 Stone J. M., Norman M. L., 1992, *ApJS*, 80, 753
 Stone J. M., Pringle J. E., 2001, *MNRAS*, 322, 461
 Stone J. M., Pringle J. E., Begelman M. C., 1999, *MNRAS*, 310, 1002
 Tayler R. J., 1973, *MNRAS*, 161, 365
 Timmes F. X., Hoffman R. D., Woosley S. E., 2000, *ApJS*, 129, 377
 Timmes F. X., Swesty F. D., 2000, *ApJS*, 126, 501
 van Kerkwijk M. H., Chang P., Justham S., 2010, *ApJ*, 722, L157
 Webbink R. F., 1984, *ApJ*, 277, 355
 Woosley S. E., Kasen D., 2011, *ApJ*, 734, 38
 Yoon S.-C., Podsiadlowski P., Rosswog S., 2007, *MNRAS*, 380, 933

APPENDIX A: VERIFICATION TESTS

We perform a number of tests to confirm that our results are insensitive to the details of our approximations and numerical methods. A summary of these test runs is shown in Table A1. Each run has an ID, which begins ZT n , where ZT represents “ZEUS testing” and n is an integer, indicating that SPH simulation Pn of Dan et al. (2011) was used to generate the initial conditions. The results of these tests are discussed in the following sections.

A1 Resolution

We confirm that our solutions are numerically converged by performing runs at different resolutions. We perform runs with 2/3 and 4/3 the linear resolution of the fiducial calculation. Fig. A1 shows 1D profiles from each of these runs after 10^4 s. There is only a small variation between the fiducial run (ZP5) and the high resolution run (ZT5-HR). The lower resolution run (ZT5-LR) also agrees quite well; the visible variation is in the interior of the surviving WD, not the viscously evolving exterior. These results demonstrate that our simulations are converged in the quantities of interest.

ID	Parameter	Value
ZT5-LR	N_r, N_θ	48,32
ZT5-HR	N_r, N_θ	96,64
ZT5-alpha-m	α	10^{-2}
ZT5-alpha-p	α	10^{-1}
ZT5-hydro	α -viscosity	Off
ZT5-visc-full	α -viscosity	All components
ZT2-burn-ap13 [†]	Network	aprox13
ZT2-burn-heco [†]	Network	HeCONE
ZT2-burn-off [†]	Network	No Burning
ZT5-IC1	$t_{\text{end,SPH}}$	$35 P_0$
ZT5-IC2	$t_{\text{end,SPH}}$	$35.6 P_0$
ZT5c-rnu-m	r_ν	$2.5 \times 10^8 \text{ cm}$
ZT5c-rnu-p	r_ν	$5.0 \times 10^8 \text{ cm}$

Table A1. Details of the test runs discussed in this appendix. ID is the run ID: ZT represents “ZEUS testing” and the number indicates which initial conditions are being simulated. The string following the first dash briefly describes the parameter being changed. Parameter is a description of the aspect of the run that was varied. Value is its value. [†]this simulation had a lower resolution, $N_r, N_\theta = 48, 32$

A2 Independence of α

We expect our simulations to be insensitive to the exact value of α so long as the hierarchy of time-scales in the problem remains unchanged. Specifically, α must not be so small that energy transport by radiation (or energy release from nuclear reactions) becomes important and not so large that the viscous time becomes less than the orbital time. Fig. A2 shows that we observe only weak variation in our results with α in the range 0.01 – 0.1. The simulations are compared after a constant number of viscous times, such that $\alpha t_{\text{end}} = 3 \times 10^2 \text{ s}$.

A3 Viscosity Tensor

Motivated by numerical simulations of the MRI we choose a prescription in which only the azimuthal components of the viscous shear tensor were retained. We relax this assumption and explore the effects of retaining all components of the tensor. This choice has virtually no effect on the evolution of the material near the temperature peak, as the large initial ϕ velocity shear means that the non-azimuthal components of the tensor are small in comparison anyways. In the outer regions where azimuthal shear is not always so dominant, this choice can have an effect. In the fiducial case the evolution of the outer $\sim 0.2 M_\odot$ of material shows some minor differences. However, none of our conclusions are based on the detailed structure of the outer material, so this does not alter any of our conclusions.

A4 Initial Conditions

In order to confirm that our results are independent of small details of the initial conditions, we initialize our simulations with output from the same SPH calculation taken at three different times. By default, we start from the end of the SPH

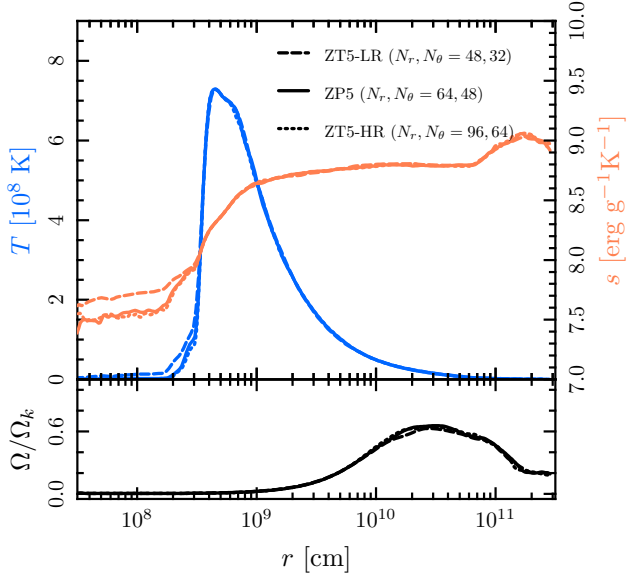


Figure A1. The convergence of our simulations of the fiducial remnant with numerical resolution. The top panel shows 1D temperature and entropy profiles and the bottom panel shows the ratio of the angular velocity to the Keplerian angular velocity. The overlap of the fiducial run (ZP5) and the high resolution run (ZT5-HR) indicate our simulations are converged in these quantities.

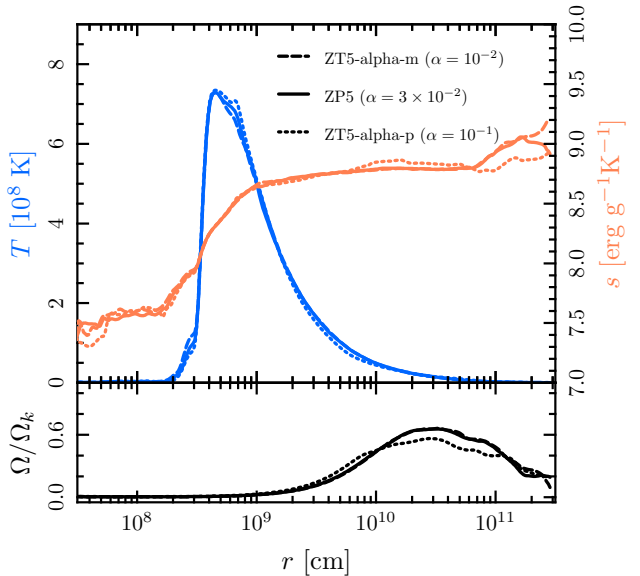


Figure A2. The variation of our simulations of the fiducial remnant with different values of α . The profiles are shown after the same number of viscous times, at $\alpha t_{\text{end}} = 3 \times 10^2 \text{ s}$. While there are small variations between runs, we see no significant change in our results for values of α spanning an order of magnitude.

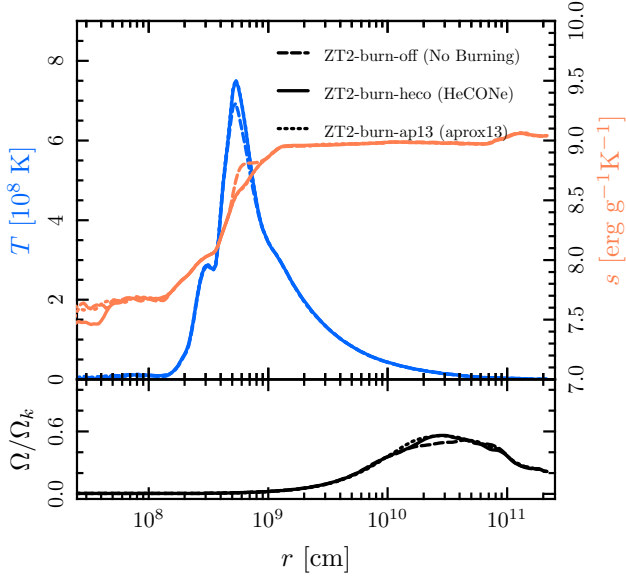


Figure A3. The variation of our simulations of the $0.3 + 1.1M_{\odot}$ remnant with different nuclear networks. The top panel shows 1D temperature and entropy profiles and the bottom panel shows the ratio of the angular velocity to the Keplerian angular velocity. The results of our simple network (HeCONE) and the aprox13 network are almost indistinguishable. We show the results of omitting the network entirely to illustrate the small impact of nuclear burning on the remnant structure over the viscous time-scales of interest.

calculation, which for the fiducial model was after 35.7 initial orbital periods had elapsed. (The secondary was tidally disrupted after 29 orbits.) The results we obtain with initial conditions from output taken 0.1 and 0.7 initial orbital periods before the end of the calculation are virtually identical. The outcome of our calculation is insensitive to the duration of the SPH simulation, so long as the remnant has had sufficient time to evolve towards axisymmetry.

A5 Viscosity Cutoff

As expected, we confirm that our results are insensitive to the location of the cutoff radius defined in Equation 6 and the surrounding discussion.

A6 Nuclear Network

As discussed in Section 2.3 we implement a simple 5 isotope (He, C, O, Ne, Mg) nuclear network. We confirm that this simple nuclear network reproduces the results of the more sophisticated aprox13 network. Because of the high computational cost of the full network, we perform these test calculations at a lower resolution. We perform these tests on the $0.3 + 1.1$ He+CO system (ZP2) as it has the shortest burning time of any of the He+CO mergers we consider. Fig. A3 shows that the two networks give identical results. We also show the effect of omitting the nuclear burning, which does change the values of the thermodynamic quantities near the temperature peak, but does not alter the overall structure of the remnant.

A7 3D

Moving to 3D makes the viscous evolution substantially more computationally demanding because of the strong timestep constraint imposed by our explicit evolution of the viscous terms, $\Delta t_{\text{visc}} \sim \min((\Delta r)^2/\nu)$. A zone near the pole ($\theta \approx \pi/(4N_{\theta})$) has size $\Delta r = 2\pi r \theta / N_{\phi}$, where N_{ϕ} is the number of ϕ zones. This means that at the same r, θ resolution, a 3D calculation will require evolving approximately N_{ϕ} as many zones at timestep smaller by a factor of N_{ϕ}^2 . This issue can be helped somewhat by subcycling, that is advancing the viscous terms at Δt_{visc} but integrating the rest of the hydrodynamics at Δt_{CFL} .

In light of these issues, the simulation we perform is a simple one in which we initialize the same azimuthally symmetric initial conditions used in 2D on a lower resolution 3D grid ($N_r = 48, N_{\theta} = 32, N_{\phi} = 32$). We evolve the system for a substantially shorter time, only 1×10^2 s. Over that limited time, we observe no qualitative differences which would affect our conclusions.